Journal of Power Sources 449 (2020) 227576

Contents lists available at ScienceDirect

Journal of Power Sources

journal homepage: www.elsevier.com/locate/jpowsour

Fe–P–S electrodes for all-solid-state lithium secondary batteries using sulfide-based solid electrolytes

Yuta Fujii [a], Misaki Kobayashi [a], Akira Miura [b,*], Nataly Carolina Rosero-Navarro [b], Minchan Li [c,d], Jianguo Sun [d], Masashi Kotobuki [d], Li Lu [d], Kiyoharu Tadanaga [b]

[a] Graduate School of Chemical Sciences and Engineering, Hokkaido University, Sapporo, 060-8628, Japan
[b] Faculty of Engineering, Hokkaido University, Sapporo, 060-8628, Japan
[c] Department of Materials Science and Engineering, Southern University of Science and Technology, Shenzhen, 518055, China
[d] Department of Mechanical Engineering, National University of Singapore, Singapore, 117575, Singapore

HIGHLIGHTS

- Fe–P–S-based electrode is prepared.
- Fe–P–S-based electrode is composed of FeS_2 and amorphous P–S.
- The electrode with 2 wt% carbon additive is used for all-solid-state battery.
- The battery exhibits a reversible capacity above 625 mAh g^{-1} for 50 cycles at 100 °C.

GRAPHICAL ABSTRACT

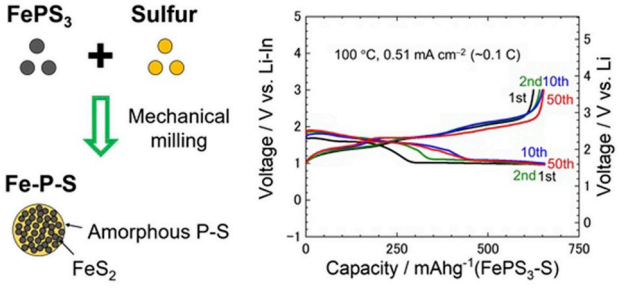

ARTICLE INFO

Keywords:
Lithium-sulfur battery
All-solid-state battery
Fe-based composite cathode material
High-capacity electrode

ABSTRACT

Although lithium-sulfur batteries are expected to be the next-generation high-capacity battery of choices, the sulfur electrodes studied so far contain large amounts (typically 30–60 wt%) of carbon additives, resulting in low energy density. In this study, an Fe–P–S-based material is prepared and characterized for the use as a sulfur electrode with a low content of carbon additives. The electrode material based on Fe–P–S is synthesized by the mechanical milling of $FePS_3$ and elemental sulfur. The ball-milled $70FePS_3{\cdot}30S$ (wt%) electrode comprises FeS_2 particles of ~30 nm in size and amorphous P–S. The all-solid-state battery operated at 100 °C exhibits a reversible capacity of more than 625 mAh g^{-1} for 50 cycles at 0.51 mA cm^{-2} (~0.1C) in spite of the low carbon content (2 wt%) in the electrode. During the discharge-charge cycle, the sulfur component is confirmed to be both reduced and oxidized, cyclically.

1. Introduction

Lithium-ion secondary batteries have been used as power sources for portable electric devices because of their high operating voltage, high energy density, and good cycleability [1–3]. Further increase in the energy density of the batteries can be achieved by high-voltage and/or high-capacity electrodes. Elemental sulfur has attracted much attention as a high-capacity cathode material for lithium secondary batteries

* Corresponding author.
E-mail address: amiura@eng.hokudai.ac.jp (A. Miura).

https://doi.org/10.1016/j.jpowsour.2019.227576
Received 14 August 2019; Received in revised form 8 November 2019; Accepted 5 December 2019
Available online 18 December 2019

[4–6]. Although sulfur as a cathode has a low discharge potential (~2.1 V *vs*. Li), the theoretical capacity is 1672 mAh g^{-1}, which is approximately ten times higher than the capacity of $LiCoO_2$. Thus, the energy density of the lithium batteries can be increased significantly by using a high-capacity electrode composed of sulfur. One of the disadvantages of the sulfur active material is its insulating nature [7]. To form sufficient electron conducting paths, large amounts of carbon additives, typically 30–60 wt% [8,9], must be mixed with the sulfur of the electrode. The another disadvantage of the sulfur electrode active material is the rapid degradation in the battery when using liquid electrolytes due to dissolution of lithium polysulfide formed in the battery operation into the liquid electrolytes.

All-solid-state lithium secondary batteries using sulfur electrodes and non-flammable inorganic solid electrolytes have the advantage of high safety [10]. Needless to say, lithium polysulfides do not dissolve into solid electrolytes, leading to long cycle life of the battery with the sulfur electrode. However, in all-solid-state batteries, the formation of sufficient lithium-ion paths as well as a large contact area between electrodes and electrolytes is difficult to achieve. To form the sufficient paths and a large contact area, solid electrolytes must be mixed with the sulfur electrode to form composite electrodes. In the same way, electron conduction paths are also formed by mixing carbon additives with the sulfur electrode. Since all the components in the all-solid-state batteries are solids, it is not easy to create enough conduction paths so that the all-solid-stat battery can only be operated at a low discharge-charge rate (for ~0.1C). For example, all-solid-state batteries using sulfur composite electrodes such as Cu–S [10] and C–FeS_2–S [11] were operated at only 0.02C even though they showed a high capacity. Although it is known that the carbon content in the sulfur electrode should be as low as possible in order to increase the volumetric and gravimetric energy density of batteries, the amount of conductive carbon used in the sulfur battery is hardly below 10 wt% due to insulating nature of sulfur. Based on the best of our knowledge, there is no literature reporting a discharge-charge rate >0.1C of all-solid-state batteries using sulfur composite electrodes with a low carbon content less than 10 wt%. Properties of the all-solid-state lithium-sulfur batteries using sulfur or sulfur composite cathode materials reported in previous literatures are tabulated in Table S1. The low C-rate may be related to low ionic and electronic conductivities in the sulfur electrode. Interestingly, these conductivities can be enhanced by increasing the temperature. High-temperature operation, which is the advantage of a solid electrolyte over a liquid electrolyte because of no evaporation nature of the solid electrolyte, would allow an all-solid-state battery to exhibit a discharge-charge profile with a reasonable discharge and charge rate.

Metal sulfides (e.g. TiS_2 [12], MnS [13], FeS [14], $FePS_3$ [15,16], NiS [17], $NiPS_3$ [15,18], CuS [19], and MoS_2 [20]) have been investigated as electrode active materials for lithium secondary batteries. Among them, metal sulfides such as TiS_2 and $FePS_3$, which have layered structures, exhibit the lithium-ion insertion/extraction reaction [21]. The electronic conductivities of TiS_2 and $FePS_3$ are 1.2×10^2 and $\sim 10^{-5}$ S cm^{-1}, respectively [22,23]. The theoretical capacities of TiS_2 and $FePS_3$ are 239 and 220 mAh g^{-1}, respectively, which are lower than those of other metal sulfides showing conversion reactions. To increase the capacity, we focused on mixing the metal sulfide with sulfur electrode active material. The sulfur composite electrode which contains the metal sulfide has a moderate electronic conductivity and is expected to possess electron paths without the addition of large amounts of carbon additives. The large volume change of the sulfur electrode, which is responsible for the degradation for these types of batteries, can be reduced by the inclusion of metal sulfides because of the smaller volume change of the metal sulfides. Moreover, stable electrode-electrolyte interfaces are expected to be formed even at high temperatures because of the similarity of the composition of sulfur in the sulfur composite electrodes and sulfide-based solid electrolytes. For the S-based batteries using liquid electrolytes, some composites such as Li_2S-*M* (*M* = Co, Fe) [24], Li_2S-MS_2 (*M* = Ti, V, Zr, Mo) [25,26], Li_2S-FeS_x [27], and Li_2S–$FePS_3$ [28] have been developed as cathode materials. Transition-metal polysulfides (*e.g.* MS_3 (*M* = Ti [29,30], Nb [31], Mo [32,33]), Li_2TiS_3 [34], $MoS_{3.4}$ [35], MS_4 (*M* = Ti [36], V [37], Nb [31]), Li_2WS_4 [38], Li_3NbS_4 [34], M_3S_4 (*M* = Fe [39], Ni [40]), NbS_5 [31], and $MoS_{5.7}$ [41] have attracted much attention as another family of cathode materials possessing high theoretical capacity based on the redox reaction of sulfur and/or transition metals.

In addition to studies on these composite cathode materials, the composite cathode materials that are suitable for all-solid-state batteries such as Li_2S–Cu [42], Li_2S–P_2S_5–Cu [43], and C–FeS_2–S [11] have also been studied. Considering the more abundant element in the earth's crust, an iron-based metal sulfide would be economical to be used as the additive for a sulfur electrode. However, in the all-solid-state batteries, few composite cathode materials consisting of sulfur and an iron-based metal sulfide have been investigated so far [11]. Moreover, there are not many reports on the operation of the all-solid-state batteries using sulfide-based solid electrolytes at a high temperature (100 °C) [44–47], even though the evaluation of the battery performance at 100 °C is useful for the practical all-solid-state lithium-sulfur batteries in terms of the faster lithium dissolution-deposition process at the high temperature than a room temperature.

In the present study, we developed new electrode systems for all-solid-state batteries by simple mixing an iron-based metal sulfide with sulfur, and investigated the performance of the new electrode materials in batteries at 100 °C. Among iron-based metal sulfides, we focused on $FePS_3$ containing a P–S unit, which has been reported as an electrode active material [48,49]. Since the addition of P_2S_5 to a sulfur electrode has been reported to improve the performance of batteries [50], the mixture of $FePS_3$ with the sulfur electrode in our batteries is expected to obtain superior performance.

In this study, new Fe–P–S electrodes were synthesized by mechanical milling of $FePS_3$ and S, and the electrochemical performance of the Fe–P–S electrodes with a liquid or solid electrolyte was investigated.

2. Experimental

Fe–P–S electrodes were synthesized by mechanical milling of $FePS_3$ and sulfur (Kanto Chemical, 99.5%). $FePS_3$ was synthesized by heating a mixture of iron powder (Wako Chemical, 99.9%), red phosphorus (Kanto Chemical, 98.0%), and sulfur (Kanto Chemical, 99.5%) [16,48]. The synthesized $FePS_3$ and elemental sulfur were mixed using an agate mortar with weight ratio of 100:0, 70:30, and 50:50, respectively. Then, the mixtures were mechanically milled using a planetary ball mill (Fritsch, Pulverisette 7) with a zirconia pot (45 mL volume) and 500 zirconia balls ($\varphi = 4$ mm) in a dry Ar atmosphere at 510 rpm for 24 h. To identify the crystalline structures of the resultant powder of the $70FePS_3{\cdot}30S$ electrode, an X-ray diffraction (XRD) pattern was recorded using an X-ray diffractometer (Miniflex 600, Rigaku) under Cu-Kα radiation. For this measurement, a sample stage was covered with Kapton film to avoid undesired reaction of the samples with air. A Raman spectrum of the milled powder of the $70FePS_3{\cdot}30S$ electrode was measured using a Raman spectrometer (XploRA, Horiba) with a green laser (Wavelength: 532 nm) to identify the structural units. For the Raman measurement, the sample was sealed in an evacuated capillary glass tube. The morphology and elemental mapping were studied using focused ion beam–scanning electron microscopy (FIB-SEM; JIB-4600, JEOL) and scanning transmission electron microscopy (STEM; HD-2000, Hitachi) in conjunction with an energy dispersive spectroscopy (EDS) system. The stability of the $70FePS_3{\cdot}30S$ electrode at high temperature was evaluated by thermogravimetric and differential thermal analysis (TG-DTA; Thermo Plus TG 8120, Rigaku). The electronic conductive of the $70FePS_3{\cdot}30S$ electrode was measured using a symmetric stainless steel/$70FePS_3{\cdot}30S$/stainless steel cell.

All-solid-state batteries (Li–In/$75Li_2S{\cdot}25P_2S_5$ (mol%) glass/Fe–P–S) were assembled as described in a previous paper [51]. $75Li_2S{\cdot}25P_2S_5$ (mol%) glass solid electrolytes were prepared by mechanical milling of

Li_2S (Mitsuwa Chemical, 99.9%) and P_2S_5 (Aldrich, 99%) [52]. The Li_2S and P_2S_5 powders were mixed together using an agate mortar, and the mixture was placed into ZrO_2 pots (45 mL) with 500 ZrO_2 balls (φ = 4 mm). The pots were set in a planetary ball mill apparatus (Fritsch, Pulverisette 7), and mechanical milling was performed at 510 rpm for 24 h. Cathode composite electrodes were prepared by mixing the Fe–P–S electrode samples, the $75Li_2S{\cdot}25P_2S_5$ (mol%) glass, and vapor-grown carbon fibers (VGCF, Showa Denko) in a weight ratio of 69:29:2 (wt %). To measure the electronic conductivity of the composite electrode, a symmetric stainless steel/composite electrode/stainless steel cell was constructed. The composite electrodes (10 mg) and the $75Li_2S{\cdot}25P_2S_5$ (mol%) glass solid electrolytes (120 mg) were placed into a polycarbonate tube (φ = 10 mm), and pressed under 360 MPa. A Li–In alloy foil was attached to the bilayer pellet consisting of the cathode composite electrode and the solid electrolyte layers by uniaxially pressing them together at 120 MPa. These pellets were sandwiched by two stainless-steel disks as current collectors. The assembled all-solid-state batteries were discharged and charged under a constant current density of 0.51 mA cm^{-2} at different temperatures (25, 60, 80, and 100 °C) using a discharge-charge measuring device (Scribner Associates, 580 battery-type system). The discharge-charge measurement was initiated with discharge. To evaluate the rate performance of the battery, the constant current densities from 0.51 to 8.15 mA cm^{-2} were used for the discharge cycles.

To compare the performance of the all-solid-state battery with that of the battery using liquid electrolytes, the battery (Li/Fe–P–S) using liquid electrolytes was also constructed. In a typical processing, the Fe–P–S electrode sample of $70FePS_3{\cdot}30S$, polyvinylidene fluoride (PVDF), and Super P carbon were mixed using an agate mortar in a weight ratio of 75:15:10 (wt%). Subsequently, 1-methyl-2-pyrrolidone (NMP) was added to the mixture to prepare a slurry. This slurry was loaded onto a copper foil and dried at 100 °C for 24 h in a vacuum. A CR2016 coin-cell battery was constructed using the dried composite cathode foil as a working electrode, porous propylene separator (Celgard 2500), 1 M $LiPF_6$ in ethylene carbonate (EC)/dimethyl carbonate (DMC)/diethyl carbonate (DEC) (1:1:1, wt/wt/wt%) as a liquid electrolyte, and Li foil as reference and counter electrodes. The weight of the $70FePS_3{\cdot}30S$ sample was 0.575 mg cm^{-2}. The cell was discharged and charged at a constant current density of 65.6 mA g^{-1} (~0.1C) at room temperature (typically 25–30 °C), using a discharge-charge mechine (LANHE CT2001A). The discharge-charge measurement was initiated with discharge.

To examine the reaction mechanism of the $70FePS_3{\cdot}30S$ electrode, the products of the $70FePS_3{\cdot}30S$ composite electrode in the all-solid-state batteries after the charge cycles were investigated by the XRD measurement. To reveal the redox reaction of the $70FePS_3{\cdot}30S$ electrode during discharge-charge cycles, the S *K*-edge X-ray absorption near edge structure (XANES) spectra of the cathode composite electrode in the all-solid-state batteries were measured before and after discharge/charge. XANES spectra were measured at the BL6N1 (proposal No. 201705058) of the Aichi Synchrotron Center, Aichi Science & Technology Foundation. K_2SO_4 was used as a standard sample for XANES measurement to calibrate the spectra data. Their intensity was normalized as zero and one for the intensity at 2466.4 eV and 2489.5 eV, respectively. These processes were all performed under a dry Ar atmosphere.

3. Results and discussion

Fig. 1 shows the XRD patterns of the Fe–P–S electrode of $70FePS_3{\cdot}30S$. For comparison, the XRD spectra of pyrite FeS_2, reagent-grade sulfur, and the prepared $FePS_3$ are also shown in Fig. 1. The diffraction peaks of the XRD pattern of $70FePS_3{\cdot}30S$ are attributed to pyrite FeS_2 (ICSD #316) without peak shift. Considering the composition of the $70FePS_3{\cdot}30S$ electrode, this result indicates that the $70FePS_3{\cdot}30S$ electrode is composed of the pyrite FeS_2 phase and amorphous phase(s) containing phosphorus and sulfur.

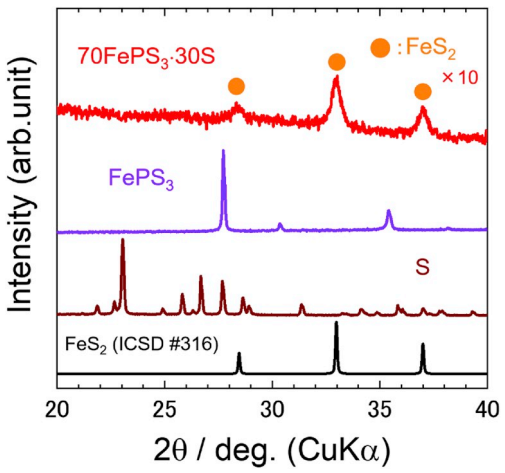

Fig. 1. XRD patterns of the Fe–P–S electrode of $70FePS_3{\cdot}30S$, $FePS_3$ before mechanical milling, reagent-grade pure sulfur and PDF file of FeS_2.

Fig. 2 shows the Raman spectrum of the $70FePS_3{\cdot}30S$ electrode. Raman bands present at 337 and 373 cm^{-1} are similar to those attributed to S^{2-} in FeS_2 [53]. These results are in agreement with the XRD result, in which only the FeS_2 pyrite phase is detected. In the Raman spectrum, a band at 412 cm^{-1} is also noted. It has been reported that P–S bonds in $P_2S_6^{4-}$, $P_2S_7^{4-}$, and PS_4^{3-} units show Raman bands at 390, 410, and 425 cm^{-1}, respectively [54,55]. Therefore, the observed band at 412 cm^{-1} could be attributed to the P–S bond of the $P_2S_7^{4-}$ unit in amorphous phase(s) containing phosphorus and sulfur.

Fig. 3 (a) through (e) present an SEM and a HAADF-STEM image, and EDS mapping of Fe, P, and S of the $70FePS_3{\cdot}30S$ electrode, respectively. The particle size of the $70FePS_3{\cdot}30S$ electrode is in the range of 1–5 μm (Fig. 3 (a)). The STEM image of the $70FePS_3{\cdot}30S$ electrode particle as shown in Fig. 3(b) reverals bright and dark features, suggesting that the $70FePS_3{\cdot}30S$ particle is composed of two or more component phases. Indeed, iron and phosphorus in the $70FePS_3{\cdot}30S$ particle are non-uniformly distributed (Fig. 3 (c) and (d)) while sulfur is uniformly distributed (Fig. 3 (e)). In the mapping image of iron (Fig. 3 (c)), the distribution of iron corresponds mainly to the bright regions of the HAADF-STEM image (Fig. 3 (b)), with an average size of approximately 30 nm. Considering SEM and STEM images, and the XRD results, $70FePS_3{\cdot}30S$ contains FeS_2 with a particle size of approximately 30 nm. However, we cannot deny the possibility of P doping into FeS_2, because a very similar case of P-doped CoS_2, isostructural to FeS_2, has been reported [56,57]. Other components in the $70FePS_3{\cdot}30S$ particle, which correspond to darker regions in Fig. 3 (b), are amorphous phase(s)

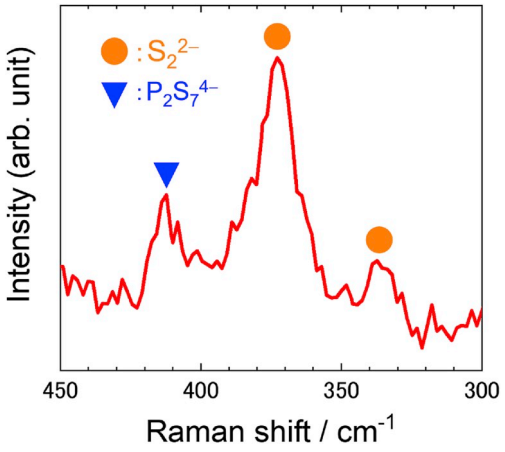

Fig. 2. Raman spectrum of the $70FePS_3{\cdot}30S$ electrode.

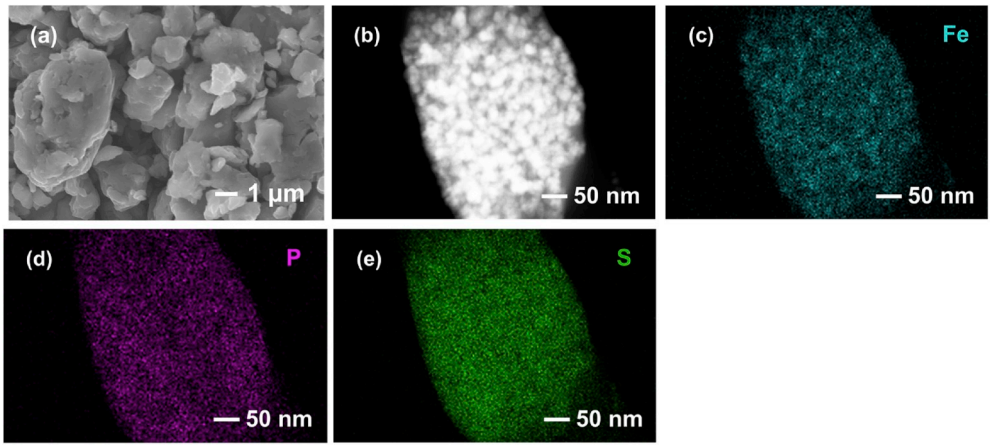

Fig. 3. (a) SEM image, (b) HAADF-STEM image, and EDS mapping of (c) Fe, (d) P, and (e) S of the 70$FePS_3$·30S electrode.

composed of phosphorus and sulfur. The electronic conductivity of the 70$FePS_3$·30S electrode is 3×10^{-7} S cm^{-1} at 27 °C and 6×10^{-6} S cm^{-1} at 100 °C, which are much higher than that of sulfur (5×10^{-18} S cm^{-1} at 20 °C) [7]. In the TG-DTA curves (Fig. S1), no siginificant change in weight and heat are seen below 120 °C, suggesting that the 70$FePS_3$·30S electrode neither showed evaporation and melt.

Fig. 4 shows discharge-charge curves of the all-solid-state battery using the 70$FePS_3$·30S electrode at 25 °C (Fig. 4 (a)) and the battery with 70$FePS_3$·30S and the liquid electrolytes at room temperature (typically 25–30 °C) (Fig. 4 (b)). The current densities of 0.51 mA cm^{-2} (~0.1C) for the all-solid-state battery and of 65.6 mA g^{-1} (~0.1C) for the battery with liquid electrolytes were used. The all-solid-state battery exhibits discharge-charge capacity of less than 1 mAh g^{-1} at 25 °C. The low capacity could be attributed to the low electronic conductivity of 5×10^{-7} S cm^{-1} of the composite electrode with Li–P–S electrolyte and 2 wt % carbon additive. In contrast, the first charge capacity of the battery using the liquid electrolyte is 414 mAh g^{-1}. Note that the capacity of the battery with liquid electrolytes cannot be directly compared with that of the all-solid-state battery because of the different amounts of carbon additives. More importantly, its capacity, however, degrades rapidly with repetition of the discharge-charge cycles. From the 10th cycle onwards, the discharge capacity is less than 15 mAh g^{-1} because of the dissolution of the polysulfide [58].

In order to achieve large discharge-charge capacity at a reasonable rate, we examined the discharge-charge performance of the all-solid-state battery at 100 °C. In the preliminary experiment of the discharge-charge measurements at different temperatures (25, 60, 80, and 100 °C), shown in Fig. S2, the all-solid-state battery heated at 100 °C exhibits the high reversible capacity of 625 mAh g^{-1} for the first cycle. Fig. 5 (a) shows discharge-charge curves of the all-solid-state battery with the 70$FePS_3$·30S electrode at 100 °C, under a current density of 0.51 mA cm^{-2} (~0.1C). In the discharge-charge measurement, the battery is firstly discharged with a capacity of 656 mAh $g^{-1}_{(Fe–P–S)}$. Subsequently, the battery is charged to 3.0 V *vs.* Li–In. The capacity of 656 mAh $g^{-1}_{(Fe–P–S)}$ is calculated by using the theoretical capacities of $FePS_3$ (220 mAh g^{-1}) and sulfur (1672 mAh g^{-1}) with the weight ratio of 70:30, but the theoretical capacity of the 70$FePS_3$·30S electrode is different to this capacity (656 mAh g^{-1}). The theoretical capacity can be estimated based on final products of FeS_2 and amorphous P–S. If 70 wt% $FePS_3$ and 30 wt% sulfur (1 mol $FePS_3$ and 2.4 mol sulfur) in the original composite react completely by mechanical milling process, the weight ratio of FeS_2 and amorphous P–S can be estimated to be 46:54 (wt%) based on this reaction. The theoretical capacity of FeS_2 is 894 mAh g^{-1}. In regarding to the amorphous P–S, the composition of P and S can be estimated to be 1:3.4 (mol) based on the reaction of 70 wt% $FePS_3$ with 30 wt% sulfur. If the amorphous $PS_{3.4}$ reacts with Li completely and Li_3P and Li_2S are formed, the theoretical capacity can be calculated to be 1876 mAh g^{-1}. By using the estimated weight ratio (46:54 (wt%)) and these theoretical capacities (FeS_2: 894 mAh g^{-1} and $PS_{3.4}$: 1876 mAh g^{-1}), the theoretical capacity of the 70$FePS_3$·30S electrode would be 1423 mAh $g^{-1}_{(Fe–P–S)}$. The battery shows stable reversible discharge-charge behavior for 50 cycles in spite of the low content of the carbon additive (2 wt%) in the 70$FePS_3$·30S composite electrode.

During the first discharge curve, two plateaus at ~1.0 and ~1.7 V *vs.*

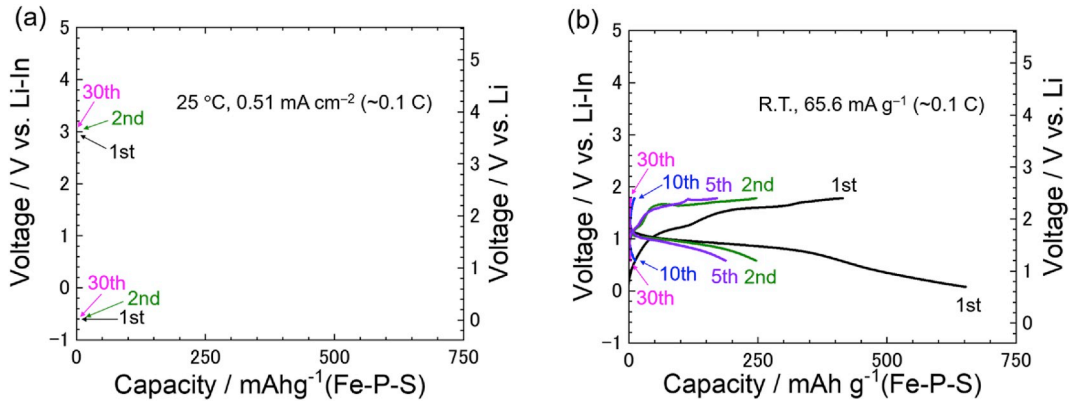

Fig. 4. Discharge-charge curves of (a) all-solid-state battery using the 70$FePS_3$·30S electrode at 25 °C and (b) battery with the 70$FePS_3$·30S and liquid electrolytes at room temperature (typically 25–30 °C). In the all-solid-state battery, the cut-off voltage was set to −0.62 V vs. Li–In for discharging and 3.0 V vs. Li–In for charging. 1 C-rate was defined as 5.8 mA cm^{-2} required to (dis)charge the battery in 1 h. On the other hand, the battery with liquid electrolytes was firstly discharge to a capacity of 656 mAh g^{-1}. From the first charge cycle onwards, the cut-off voltage was set to 1.78 V vs. Li–In for charging and 0.58 V vs. Li–In for discharging.

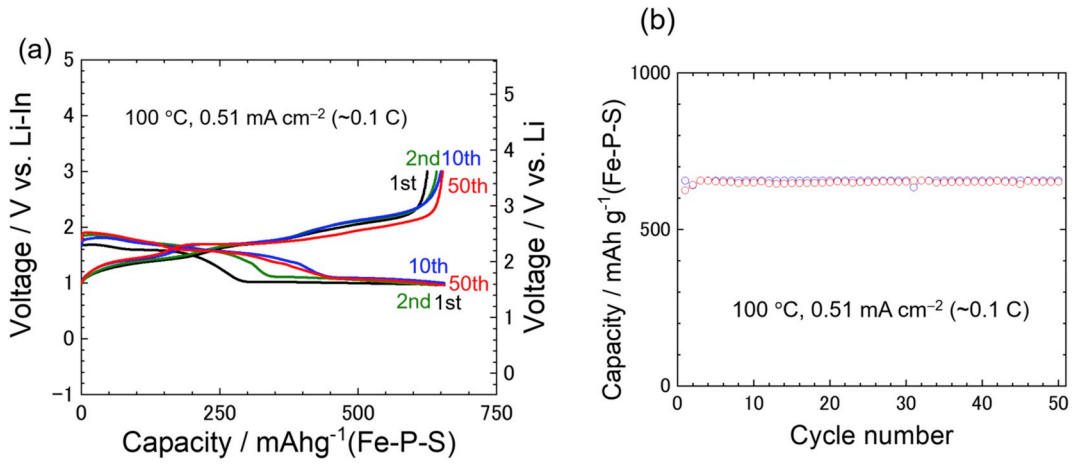

Fig. 5. (a) Discharge-charge curves and (b) cycle performance of the all-solid-state battery using the $70FePS_3{\cdot}30S$ electrode at 100 °C under a current density of 0.51 mA cm^{-2} (~0.1C). Discharge and charge capacities are represented by blue and red dots, respectively. For discharging, the cut-off voltage was set to 0.9 V vs. Li–In and the cut-off capacity was set to 656 mAh g^{-1}. For charging, the cut-off voltage was set to 3.0 V vs. Li–In. 1 C-rate was defined as 5.8 mA cm^{-2} required to (dis) charge the battery in 1 h. (For interpretation of the references to color in this figure legend, the reader is referred to the Web version of this article.)

Li–In are observed. Sulfur has been reported to show two plateaus [59, 60]. The plateau at ~1.7 V *vs.* Li-In is attributed to the reduction of sulfur to Li_2S_n ($n > 4$). The another plateau at ~1.5 V *vs.* Li-In corresponds to the further reduction of Li_2S_n to Li_2S_2 or Li_2S. The observed plateau at ~1.7 V *vs.* Li–In in a range of capacities from 0 to ~280 mAh g^{-1} can be attributed to the redox reaction of sulfur in amorphous phase (s) containing phosphorus and sulfur. On the other hand, the plateau at ~1.0 V *vs.* Li–In in a range of capacities from ~280 to ~660 mAh g^{-1} can correspond to the redox reactions of Fe^{2+} and S_2^{2-} in FeS_2 because FeS_2 exhibits a discharge plateau at 0.9 and 1.1 V vs. Li-In in the redox reactions of Fe^{2+} and S_2^{2-} as shown in the following equation [61,62].

$$FeS_2 + 4Li^+ + \ 4e^- \rightarrow Fe + 2Li_2S \quad (1)$$

After the first cycle, the discharge capacity corresponding to the redox reaction of sulfur in the amorphous phase(s) is around 280 mAh g^{-1}. The sulfur utilization based on the additional amount of sulfur is 56%. A possible reason for the moderate sulfur utilization is that the electron path in the composite electrode is still insufficient to increase the sulfur utilization drastically; the electronic conductivity of the composite electrode is 1×10^{-5} S cm^{-1} at 100 °C. On the other hand, the discharge capacity attributable to the redox reactions of S_2^{2-} and Fe^{2+} in FeS_2 is around 380 mAh g^{-1}. The utilization based on the amount of FeS_2 is 92%. From the 1st to 10th cycle, the discharge profile changed gradually, and the discharge voltage in a range of capacities from ~220 to ~450 mAh g^{-1} slightly increased. For the batteries using FeS_2, the discharge voltage has been reported to increase from the second cycle onwards because of the complex reaction of FeS_2 forming FeS_x and S partially [61,62]. In the XRD pattern of the $70FePS_3{\cdot}30S$ electrode composite electrode after the charge cycles (Fig. S3), the peaks can be assigned as S, Fe_7S_8, Li_2FeS_2, $Li_4P_2S_6$, and the unknown phase(s) are observed. This result for the products of S, Fe_7S_8, and Li_2FeS_2 is consistent with the previously reported complex reaction of FeS_2 forming FeS_x and S [61,62]. $Li_4P_2S_6$ and unknown phase(s) could be formed by the reaction of the amorphous P–S with Li^+. From these results, the observed profile change can be attributed to not the redox reaction of sulfur in amorphous P–S but mainly the redox reaction in FeS_2.

Fig. 5(b) shows the cycle performance of the all-solid-state battery using the $70FePS_3{\cdot}30S$ electrode. The reversible capacity is more than 625 mAh g^{-1}, and the charge capacity at the 50th cycle is 653 mAh g^{-1}. At 100 °C, the battery shows better cycle performance than at 25 °C. The battery exhibited the discharge capacity of larger than 581 mAh g^{-1} at the current density of 2.03 mA cm^{-2} while the battery hardly showed discharge-charge behavior at the current density of equal or higher than 4.07 mA cm^{-2} (Fig. S4). We also investigated the effect of composition ratios of $FePS_3$ and S on the capacities of all-solid-state batteries operated at 100 °C, and find that $70FePS_3{\cdot}30S$ shows higher capacity than those of $100FePS_3{\cdot}0S$ and $50FePS_3{\cdot}50S$ (Fig. S5).

To clarify the discharge-charge behavior, the redox reaction of sulfur in the $70FePS_3{\cdot}30S$ electrode was further investigated. Fig. 6 shows the sulfur *K*-edge XANES spectra of the $70FePS_3{\cdot}30S$ composite electrode at different discharge-charge conditions marked as colored circles in a first discharge-charge curve of the all-solid-state battery using the $70FePS_3{\cdot}30S$ electrode. For comparison, the spectra of the $75Li_2S{\cdot}25P_2S_5$ glass solid electrolyte (Fig. 6 (A)) and sulfur (Fig. 6 (B)) are also shown. Moreover, the intensity of the sulfur component at 2471.8 eV, at which shows a strong absorption of elemental sulfur, is shown on the lower right side in Fig. 6 to discuss the chemical state of the sulfur component during the discharge-charge cycle. The samples contain some amounts of $75Li_2S{\cdot}25P_2S_5$ glass of a solid electrolyte layer. The absorption at 2471.8 eV is attributed to sulfur, whereas the absorption at 2470.8 eV is probably attributable to the $75Li_2S{\cdot}25P_2S_5$ glass. The absorption of the $75Li_2S{\cdot}25P_2S_5$ glass cannot be used for discussion in detail, because some amount of $75Li_2S{\cdot}25P_2S_5$ glass of a solid electrolyte layer was unintentionally mixed in the composite electrode samples when the measurement samples were collected. Before discharge and charge, the sulfur component is confirmed (left side in Fig. 6 (a)). At 1.1 V *vs.* Li–In during the first discharge, the peak intensity of the sulfur component decreases, as shown in the intensity at 2471.8 eV (right lower side in Fig. 6). This suggests that the sulfur component be chemically reduced during the discharge cycle up to 1.1 V *vs.* Li–In. After the first discharge, the peak intensity of the sulfur component is not significantly changed. This means the chemical state of sulfur was not significantly altered during the discharge from 1.1 V *vs.* Li–In to after the first discharge. After the first charge, the peak intensity of the sulfur component becomes stronger, as shown in the intensity at 2471.8 eV (right lower side in Fig. 6). The change of peak intensity indicates that the sulfur component is oxidized during the charge cycle. Note that the profile before discharge and charge is not completely consistent with those after the first charge. This suggests that the initial state of sulfur is not totally recovered after the charge cycle. The absorption edge energy, which is estimated at the energy of the normalized absorption intensity of 0.5, is between 2469.4 and 2469.6 eV in the spectra of the Fe–P–S composite electrodes at the all discharge-charge conditions. The absorption edge energy is almost the same as that of $75Li_2S{\cdot}25P_2S_5$ glass (2469.6 eV). This is because the samples contain some amounts of $75Li_2S{\cdot}25P_2S_5$ glass. Considering the effect of the solid electrolyte inclusion on the absorption edge energy, the redox reaction

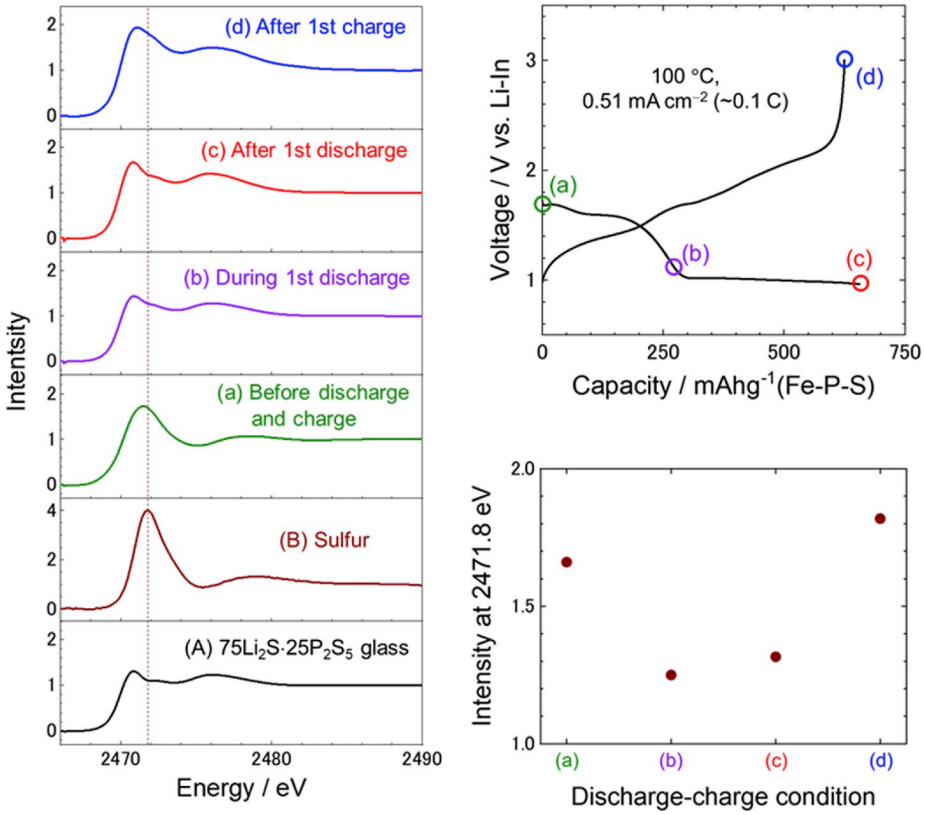

Fig. 6. Sulfur *K*-edge XANES spectra of the $70FePS_3{\cdot}30S$ composite electrode (a) before discharge and charge, (b) at 1.1 V *vs.* Li–In during the first discharge, (c) after the first discharge, and (d) after the first charge cycles. For comparison, the spectra of (A) the $75Li_2S{\cdot}25P_2S_5$ glass solid electrolytes and (B) sulfur are shown. The brown dotted line indicates the energy at 2471.8 eV corresponding to the sulfur component. First discharge-charge curve of the all-solid-state battery using the $70FePS_3{\cdot}30S$ electrode is also shown in the right upper figure. Colored circles are from the S *K*-edge XANES spectra of the $70FePS_3{\cdot}30S$ composite electrode, as measured (a) before discharge and charge, (b) at 1.1 V vs. Li–In during the first discharge, (c) after the first discharge, and (d) after the first charge cycles. Intensities at 2471.8 eV at each discharge-charge condition are shown in the right lower panel. (For interpretation of the references to color in this figure legend, the reader is referred to the Web version of this article.)

of the sulfur cannot be discussed based on the absorption edge energy. In the post-edge region of the Fe–P–S composite electrodes, the peak is observed at 2478.6 eV before discharge and charge, which is similar to that of (B) sulfur [28]. On the other hand, at 1.1 V *vs.* Li–In during the first discharge, the peak is observed at 2476.0 eV, which is consistent with that of (A) $75Li_2S{\cdot}25P_2S_5$ glass. These results indicate the sulfur component is chemically reduced during the discharge cycle up to 1.1 V *vs.* Li–In. After the first discharge and the first charge cycles, the same peak at 2476.0 eV is observed. This suggests that the sulfur component does not show the redox reaction from the discharge cycle below 1.1 V vs. Li–In to the end of the first charge cycle. Note that this result may be affected by the solid electrolyte inclusion in the samples. From the change of the absorption of sulfur *K*-edge XANES spectra, it is reasonable to conclude that the sulfur component is reduced and oxidized during the discharge-charge cycles.

In this study, the all-solid-state battery using the Fe–P–S electrode synthesized from 70 wt% $FePS_3$ and 30 wt% sulfur exhibits a reversible capacity of more than 625 mAh $g^{-1}_{(Fe-P-S)}$ mainly based on the redox reaction of sulfur in spite of low content of carbon additive (only 2 wt%) in the electrode. This is because the addition of $FePS_3$ into sulfur helped to ensure the electronic path in the electrode. The electronic conductivity of the $70FePS_3{\cdot}30S$ electrode is 3×10^{-7} S cm^{-1} at 27 °C and 6×10^{-6} S cm^{-1} at 100 °C. To compare with other all-solid-state lithium-sulfur batteries previously reported, Table S1 shows details of our battery and these batteries. The discharge capacity of 625 mAh $g^{-1}_{(Fe-P-S)}$ in our battery using the Fe–P–S electrode is lower than those of some other all-solid-state batteries shown in Table S1 since the Fe–P–S electrode can contain partially inactive phosphorus. Note that the difference of the construction conditions of the batteries prevents the quantitative comparison of these electrochemical properties. On the other hand, we believe all-solid-state battery shows reasonably good moderate rate performance (~0.1C) and the moderate discharge capacity (625 mAh g^{-1}) at 100 °C in spite of not only low carbon content but also high active material content. In addition, because of extremely low carbon content and introduction of phosphorus, which presumably help lithium-ion conductivity, our battery shows high energy density based on volume of the composite electrode even after repeated discharge-charge cycles.

4. Conclusion

Fe–P–S electrode active materials were synthesized by mechanical milling of $FePS_3$ and elemental sulfur. The resultant $70FePS_3{\cdot}30S$ powder with particles of about 1–5 μm diameter was composed of FeS_2 with the size of 30 nm, and the amorphous P–S inclusions. In the discharge-charge measurement at 100 °C, at which liquid electrolytes are unstable, the all-solid-state battery using the $70FePS_3{\cdot}30S$ composite electrode, containing only 2 wt% carbon additives, showed excellent reversible discharge-charge behavior. The reversible capacity was more than 625 mAh $g^{-1}_{(Fe-P-S)}$ for 50 cycles at 0.51 mA cm^{-2} (~0.1C) in spite of the low content of carbon additive in the composite electrode. This capacity was mainly based on a redox reaction of the sulfur component. Thus, the addition of an iron-based metal sulfide to elemental sulfur can provide moderate electronic conductivity to sulfur, and the carbon additive content in the sulfur composite electrode can be thereby decreased. The Fe–P–S electrode with low content of carbon would be useful for a high-capacity electrode for all-solid-state lithium-sulfur batteries.

Acknowledgements

This work was partially supported by the Japan Science and Technology Agency (JST), Advanced Low Carbon Technology Research and development Program (ALCA), Specially Promoted Research for Innovative Next Generation Batteries (SPRING) project, and Grant-in-Aid for JSPS Research Fellow (18J11169).

Appendix A. Supplementary data

Supplementary data to this article can be found online at https://doi.org/10.1016/j.jpowsour.2019.227576.

References

[1] J.M. Tarascon, M. Armand, Nature 414 (2001) 359–367.
[2] M. Armand, J.M. Tarascon, Nature 451 (2008) 652–657.
[3] J.B. Goodenough, Y. Kim, Chem. Mater. 22 (2010) 587–603.
[4] P.G. Bruce, S.A. Freunberger, L.J. Hardwick, J.M. Tarascon, Nat. Mater. 11 (2012) 19–29.
[5] A. Manthiram, Y. Fu, S.H. Chung, C. Zu, Y.S. Su, Chem. Rev. 114 (2014) 11751–11787.
[6] R. Kumar, J. Liu, J.Y. Hwang, Y.K. Sun, J. Mater. Chem. 6 (2018) 11582–11605.
[7] J.A. Dean, Lange's Handbook of Chemistry, third ed., McGraw-Hill, New York, 1985.
[8] X. Ji, K.T. Lee, L.F. Nazar, Nat. Mater. 8 (2009) 500–506.
[9] J. Guo, Y. Xu, C. Wang, Nano Lett. 11 (2011) 4288–4294.
[10] A. Hayashi, T. Ohtomo, F. Mizuno, K. Tadanaga, M. Tatsumisago, Electrochem. Commun. 5 (2003) 701–705.
[11] U. Ulissi, S. Ito, S.M. Hosseini, A. Varzi, Y. Aihara, S. Passerini, Adv. Energy Mater. 8 (2018) 1801462.
[12] G. Che, K.B. Jirage, E.R. Fisher, C.R. Martin, J. Electrochem. Soc. 144 (1997) 4296–94302.
[13] Y. Liu, Y. Qiao, W.X. Zhang, Z. Li, X.L. Hu, L.X. Yuan, Y.H. Huang, J. Mater. Chem. 22 (2012) 24026–24033.
[14] T.D. Kaun, P.A. Nelson, L. Redey, D.R. Vissers, G.L. Henriksen, Electrochim. Acta 38 (1993) 1269–1287.
[15] A.H. Thompson, M.S. Whittingham, Mater. Res. Bull. 12 (1977) 741–744.
[16] Y.V. Kuzminskii, B.M. Voronin, N.N. Redin, J. Power Sources 55 (1995) 133–141.
[17] S.C. Han, H.S. Kim, M.S. Song, P.S. Lee, J.Y. Lee, H.J. Ahn, J. Alloy. Comp. 349 (2003) 290–296.
[18] Y. Suto, Y. Fujii, A. Miura, N.C. Rosero-Navarro, M. Higuchi, K. Tadanaga, J. Ceram. Soc. Jpn. 126 (2018) 568–572.
[19] J.S. Chung, H.J. Sohn, J. Power Sources 108 (2002) 226–231.
[20] N. Imanishi, K. Kanamura, Z. Takehara, J. Electrochem. Soc. 139 (1992) 2082–2087.
[21] R. Brec, G. Ouvrard, A. Louisy, J. Rouxel, A.L. Mehaute, Solid State Ion. 6 (1982) 185–190.
[22] E. Guilmeau, Y. Bréard, A. Maignan, Appl. Phys. Lett. 99 (2011), 052107.
[23] K. Ichimura, M. Sano, Synthetic Metals 45 (1991) 203–211.
[24] M.N. Obrovac, J.R. Dahn, Solid State Lett 5 (2002) A70−A73.
[25] Z.W. She, J.H. Yu, W. Li, P. Hsu, H. Wang, Y. Sun, H. Yao, Q. Zhang, Y. Cui, Nat. Commun. 5 (2014) 5017.
[26] R.V. Bugga, S.C. Jones, J. Pasalic, C.S. Seu, J. Jones, L. Torres, J. Electrochem. Soc. 164 (2017) A265–A276.
[27] T. Takeuchi, H. Kageyama, K. Nakanishi, M. Ogawa, T. Ohta, A. Sakuda, H. Sakaebe, H. Kobayashi, Z. Ogumi, J. Electrochem. Soc. 162 (2015) A1745–A1750.
[28] T. Takeuchi, H. Kageyama, M. Ogawa, K. Mitsuhara, K. Nakanishi, T. Ohta, A. Sakuda, H. Kobayashi, H. Sakaebe, Z. Ogumi, Solid State Ion. 288 (2016) 199–203.
[29] A. Hayashi, T. Matsuyama, A. Sakuda, M. Tatsumisago, Chem. Lett. 41 (2011) 886–888.
[30] N. Tanibata, T. Matsuyama, A. Hayashi, M. Tatsumisago, J. Power Sources 275 (2015) 284–287.
[31] A. Sakuda, N. Taguchi, T. Takeuchi, H. Kobayashi, H. Sakaebe, K. Tatsumi, Z. Ogumi, ECS Electrochem. Lett. 3 (2014) A79−A81.
[32] T. Matsuyama, A. Hayashi, T. Ozaki, S. Mori, M. Tatsumisago, J. Mater. Chem. 3 (2015) 14142–14147.
[33] H. Ye, L. Ma, Y. Zhou, L. Wang, N. Han, F. Zhao, J. Deng, T. Wu, Y. Li, J. Lu, Proc. Natl. Acad. Sci. U. S. A 114 (2017) 13091–13096.
[34] A. Sakuda, T. Takeuchi, K. Okamura, H. Kobayashi, H. Sakaebe, K. Tatsumi, Z. Ogumi, Sci. Rep. 4 (2014) 2–6.
[35] V.V.T. Doan-Nguyen, K.S. Subrahmanyam, M.M. Butala, J.A. Gerbec, S.M. Islam, K. N. Kanipe, C.E. Wilson, M. Balasubramanian, K.M. Wiaderek, O.J. Borkiewicz, K. W. Chapman, P.J. Chupas, M. Moskovits, B.S. Dunn, M.G. Kanatzidis, R. Seshadri, Chem. Mater. 28 (2016) 8357–8365.
[36] A. Sakuda, K. Ohara, K. Fukuda, K. Nakanishi, T. Kawaguchi, H. Arai, Y. Uchimoto, T. Ohta, E. Matsubara, Z. Ogumi, T. Okumura, H. Kobayashi, H. Kageyama, M. Shikano, H. Sakaebe, T. Takeuchi, J. Am. Chem. Soc. 139 (2017) 8796–8799.
[37] X. Xu, S. Jeong, C.S. Rout, P. Oh, M. Ko, H. Kim, M.G. Kim, R. Cao, H.S. Shin, J. Cho, J. Mater. Chem. 2 (2014) 10847–10853.
[38] A. Paolella, D. Laul, V. Timoshevskii, W. Zhu, S. Marras, G. Bertoni, A.S. Wahba, G. Girard, C. Gagnon, L. Rodrigue, B. Commarieu, A. Guerfi, R. Gauvin, M. L. Trudeau, A. Vijh, M. Armand, K. Zaghib, J. Phys. Chem. C 122 (2018) 1014–1023.
[39] J. Zheng, Y. Cao, C. Cheng, C. Chen, R.W. Yan, H.X. Huai, Q.F. Dong, M.S. Zheng, C.C. Wang, J. Mater. Chem. 2 (2014) 19882–19888.
[40] N. Mahmood, C. Zhang, Y. Hou, Small 9 (2013) 1321–1328.
[41] X. Wang, K. Du, C. Wang, L. Ma, B. Zhao, J. Yang, M. Li, X.X. Zhang, M. Xue, J. Chen, ACS Appl. Mater. Interfaces 9 (2017) 38606–38611.
[42] A. Hayashi, R. Ohtsubo, M. Tatsumisago, Solid State Ion. 179 (2008) 1702–1705.
[43] A. Hayashi, R. Ohtsubo, M. Nagao, M. Tatsumisago, J. Mater. Sci. 45 (2010) 377–381.
[44] S. Mo, P. Lu, F. Ding, Z. Xu, J. Liu, X. Liu, Q. Xu, Solid State Ion. 296 (2016) 37–41.
[45] Y. Kato, S. Hori, T. Saito, K. Suzuki, M. Hirayama, A. Mitsui, M. Yonemura, H. Iba, R. Kanno, Nat. Energy 1 (2016) 16030.
[46] M. Pan, T. Hakari, A. Sakuda, A. Hayashi, Y. Suginaka, S. Mori, M. Tatsumisago, Electrochemistry 86 (2018) 175–178.
[47] A. Kato, M. Suyama, C. Hotehama, H. Kowada, A. Sakuda, A. Hayashi, M. Tatsumisago, J. Electrochem. Soc. 165 (2018) A1950–A1954.
[48] Y. Fujii, A. Miura, N.C. Rosero-Navarro, M. Higuchi, K. Tadanaga, Electrochim. Acta 241 (2017) 370–374.
[49] Y. Fujii, A. Miura, N.C. Rosero-Navarro, Y. Mizuguchi, C. Moriyoshi, Y. Kuroiwa, M. Higuchi, K. Tadanaga, J. Electrochem. Soc. 165 (2018) A2948–A2954.
[50] H. Nagata, Y. Chikusa, J. Power Sources 329 (2016) 268–272.
[51] M. Tatsumisago, M. Nagao, A. Hayashi, J. Asian Ceram. Soc. 1 (2013) 17–25.
[52] A. Hayashi, S. Hama, H. Morimoto, M. Tatsumisago, T. Minami, J. Am. Cream. Soc. 84 (2001) 477–479.
[53] H. Vogt, T. Chattopadhyay, H.J. Stolz, Phys. Chem. Solids 44 (1983) 869–873.
[54] M. Tachez, J.P. Malugani, R. Mercier, G. Robert, Solid State Ion. 14 (1984) 181–185.
[55] F. Mizuno, A. Hayashi, K. Tadanaga, M. Tatsumisago, Adv. Mater. 17 (2005) 918–921.
[56] C. Ouyang, X. Wang, S. Wang, Chem. Commun. 51 (2015) 14160–14163.
[57] J. Zhang, Y. Liu, B. Xia, C. Sun, Y. Liu, P. Liu, D. Gao, Electrochim. Acta 259 (2018) 955–961.
[58] R.D. Rauh, F.S. Shuker, J.M. Marston, S.B. Brummer, Inorg. Nucl. Chem. 39 (1977) 1761–1766.
[59] G. He, X. Ji, L. Nazar, Energy Environ. Sci. 4 (2011) 2878–2883.
[60] J.T. Yeon, J.Y. Jang, J.G. Han, J. Cho, K.T. Lee, N.S. Choi, J. Electrochem. Soc. 159 (2012) A1308–A1314.
[61] S.S. Zhang, J. Mater. Chem. 3 (2015) 7689–7694.
[62] S.S. Zhang, D.T. Tran, Electrochim. Acta 176 (2015) 784–789.